ADVANCED ENERGY MATERIALS
www.advenergymat.de

Silicon–Carbon Nanotube Coaxial Sponge as Li-Ion Anodes with High Areal Capacity

*Liangbing Hu, Hui Wu, Yifan Gao, Anyuan Cao, Hongbian Li, James McDough, Xing Xie, Min Zhou, and Yi Cui**

There is a great interest in the development of integrated power sources for microsystems to enable continued device operation when electrical plug-in is not available. In such integrated devices, the energy density per unit area is a critical figure of merit for the power system,[1,2] in contrast to other applications such as electrical vehicles and power tools where the energy density per unit weight or volume is important. There are two major means to increase the areal capacity for power modules in integrated microelectromechanical systems (MEMS) devices. One is to use 3D battery structures, where the areal energy density effectively increases due to increase in areal mass loading.[2] The other is to use materials with high energy density per unit volume. Si has been explored as an anode material due to its large theoretical capacity (gravimetric capacity approximately 4200 mAh g^{-1} with Si and volumetric capacity >8500 mAh cm^{-3} with Si or >2000 mAh cm^{-3} with Li_xSi) and potentially low cost.[3,4] However, the large volume change during charge–discharge cycling causes capacity fading.[5,6] Recently, nanostructured Si anodes have attracted much interest. Various rational designs using Si nanomaterials have been studied in the last four years, including Si nanowires, Si nanotubes, interconnected Si nanoparticles, and hollow particles.[7–15] Carbon nanotubes and nanofibers based core–shell structures have also been demonstrated to lead to excellent capacity and cycling performance.[10,16,17] These nanostructures have large structural pore volumes to accommodate the strain in the anode during the charge–discharge process. However, the mass loading per unit area has been typically low, limited by either the fabrication process or the structure design itself. The areal mass loading for these Si nanostructures needs to be improved in order for them to be used as power sources for MEMS devices for which the energy per unit area is a critical parameter.

Dr. L. Hu, Dr. H. Wu, J. McDough, X. Xie, Prof. Y. Cui
Department of Materials Science and Engineering
Stanford University
Stanford, California, 94305, USA
E-mail: yicui@stanford.edu
Y. Gao, Prof. M. Zhou
The George W. Woodruff School of Mechanical Engineering
Georgia Institute of Technology
Atlanta, GA 30332–0405, USA
Prof. A. Cao, Dr. H. Li
Department of Advanced Materials and Nanotechnology
College of Engineering
Peking University
Beijing 100871, PR China

DOI: 10.1002/aenm.201100056

In this work, we design a structure by incorporating Si, the material with high volumetric capacity, into a 3D structure to achieve an areal capacity of approximateyl 40 mAh cm^{-2} which is around 10 times that of current lithium-ion batteries. A porous, highly conductive carbon nanotube (CNT) sponge-like structure is used as the backbone on which amorphous Si is deposited uniformly.[18] The CNTs in the sponge are well connected to provide a highly conductive pathway for electrons, while the porous structure provides effective accessibility for the electrolyte to the Si anode material. Such anodes show specific capacities as high as around 2800 mAh g^{-1} with a cutoff of 0.05–1.0 V and 1300 mAh g^{-1} with a cutoff of 0.17–1.0 V. Nanopore formation and growth in the Si shell has been identified as the primary failure mode of the Si–CNT sponge anode. The damage can be minimized by tuning the cutoff voltages: much less significant morphology changes are found if the cutoff voltage is limited to 0.17–0.6 V instead of 0.05–1 V. Under such conditions, excellent cycling performance is achieved with negligible capacity fading over 50 cycles. In conjunction with experiments, a theoretical analysis is carried out to explain the pore formation mechanism. It is demonstrated that such 3D structures can function effectively as anodes with large areal capacities in MEMS devices.

The Si–CNT films were prepared through chemical vapor deposition (CVD) of amorphous Si on porous, 3D CNT sponges (**Scheme 1**). The preparation of the CNT sponges followed a process developed in a previous work.[19] The typical thickness of the CNT sponges after peeling off from glass substrate is approximately 1 cm. To deposit Si through CVD, CNT sponges with an area of 2 mm × 2 mm were wrapped by a stainless steel mesh, which anchored the samples and allowed Si deposition. Because of the porous structure of the CNT sponges, the deposition of Si is uniform throughout the entire CNT network, from the surface to the interior of the sponges. As shown in Scheme 1, the Si sponge maintains the same overall geometrical dimensions throughout the CVD. The thickness of the Si-shell within the sponge network could be controlled by varying the CVD time.[18] For our experiments, the pressure inside the furnace was set between 40 and 100 Torr and the total CVD time was 30 min. The Si–CNT coaxial sponge is flexible, pressable and capable of withstanding mechanical sonication in solvent, indicating excellent cohesion between the CNT core and the Si shell. The total Si mass M_{Si} is calculated by measuring the difference in sponge mass before and after deposition. The CNTs are well-interconnected and form a highly conductive network and the electrical connection remains the same after the deposition.

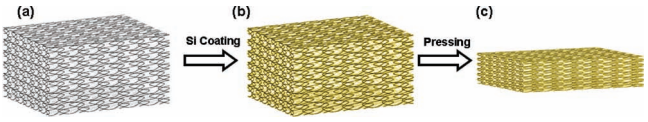

Scheme 1. a) CNT sponge used in CVD. b) Conformal CVD deposition of amorphous Si onto CNT surface to form Si–CNT coaxial nanostructure. The areal mass loading is 8 mg cm^{-2} for Si. c) Pressed Si–CNT for battery test.

The characterization of the CNT and Si-CNT sponges are shown in **Figure 1**. The Inset in Figure 1a shows the 1 cm long, 0.8 cm wide and 0.5 cm thick sponge-like structure. Such sponges can be easily cut into desirable sizes and geometries. Figure 1a shows an SEM image of the sponge with the CNTs (approximately 10 nm in diameter) entangled with each other. The CNT sponge can be compressed to less than 10% of its initial volume and springs back to its initial volume upon release of the compressive load. These highly porous and conductive backbone structures can be filled with other functional materials to form novel structures for emerging applications. The deposition of Si on the surfaces of the CNTs is essentially uniform throughout the sponge, owing to the highly porous nature of the structure. Figure 1b and c show an SEM image of a piece of a sponge after it is cut into two halves. TEM examination reveals that the amorphous Si coating around the CNTs is indeed uniform, with a thickness of around 30 nm (Figure 1d). The CNT core, which functions as the electrical pathway for the coaxial structure, is clearly seen.

The Si shell is the Li storage component. The porous nature of the sponge provides sufficient channels for the flow of electrolyte and allows excellent contact between the electrolyte and Si. To test the effectiveness of the Si–CNT sponges, coin cells were prepared with Li metal as counter electrodes. **Figure 2**a shows the voltage profile of such a cell with a cutoff voltage of 0.05–1.00 V and a charging rate of *C*/5. The first-cycle charge and discharge capacities are 3200 and 2750 mAh g^{-1} (M_{Si} is used for the capacity calculation), respecively, with a Coulombic efficiency of 86%. These high capacities are the direct result of the Si–CNT coaxial structure's effective electrical pathways and the sponge's efficient electrolyte access.

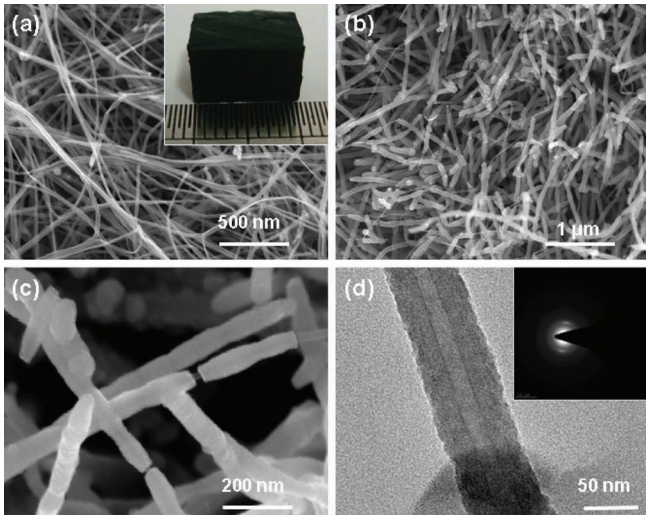

Figure 1. a) SEM image of a 3D porous CNT sponge. The CNTs are entangled and form a highly conductive network. The inset shows a picture of a CNT sponge 1 cm × 1 cm × 8 mm in size. b) SEM image of 3D porous Si–CNT sponge. c) Close-up view of (b) showing the coaxial structure of amorphous Si conformally coated around CNTs. d) TEM image of a coaxial Si-CNT structure showing the thickness of the Si coating is approximately 30 nm. The inset shows the TEM diffraction pattern of this coaxial Si–CNT structure.

The deep charge and discharge with the 0.05–1.00 V cutoff demonstates high capacity but are associated with poor cyclability (Figure 2c). To find a balance between high capacity and cyclability, the coin cells are tested with different cutoffs at the same charging rate of *C*/5. The first-cycle charge and discharge capacities for a cutoff of 0.17–1.0 V are 1800 and 1500 mAh g^{-1}, respectively, with a columbic efficiency of 83% (Figure 2b). When the discharge voltage is decreased from 1.0 to 0.6 V, the first-cycle charge and discharge capacities decrease to 1180 and 1100 mAh g^{-1}, respectively. Although the capacities are lower for the narrower operation range, the cycling performance is significantly improved, as shown in Figure 2c. It is important to note that, even at the 0.17–1.0 V cutoff, the capacities are still around 3 times those of LiC electrodes.

To characterize the failure mechanism of the core–shell structure and understand why deep charge–discharge significantly reduces cyclability, microscopic analyses were carried out after the cells were brought to the fully discharged state. The electrodes were first washed and dried before the SEM examination. **Figure 3**a shows a cross-section of a sponge after sectioning. This sample went through 50 charge–discharge cycles with a cutoff range of 1.0–0.05 V. SEM images from different areas show essentially the same morphological features of the Si–CNT coaxial structures, indicating uniform charge–discharge throughout the sponge. Figure 3b and c show two such areas, which are highlighted in Figure 3a. Figure 3d shows a TEM image of a sample with a cutoff range of 0.05–1.0 V. Clearly, nanopores have formed inside the Si–CNT shell–core structure. The nanopore formation has been observed in silicon nanowires by some of the authors previously.[20] In contrast, a sample with a cutoff range of 0.17–1.0 V shows much smoother surfaces (Figure 3e), indicating much less severe void formation. Nanopores in the Si shell may cause the Si shell to debond from the CNT core during cycling, providing an explanation for the capacity decreases with increases incycles observed in experiments. It is important to note that if the discharge voltage is further limited to 0.6 V (cutoff range of 0.17–0.6 V), the morphology change is essentially negligible. This lack of failure corresponds to the excellent cycling performance shown in Figure 2c.

The nanopore formation mechanism can be understood by an account of the inelastic deformation of Li/Si. Recent experimental evidences have indicated that Li/Si can undergo large plastic (or viscoplastic) deformations.[21] Due to the mechanical constraint imposed by the CNT core which has an elastic modulus around 10 times that of Li/Si,[22] stresses in the shell can easily exceed the elastic limit of silicon, resulting in plastic yielding (see the Supporting Information for details). Such

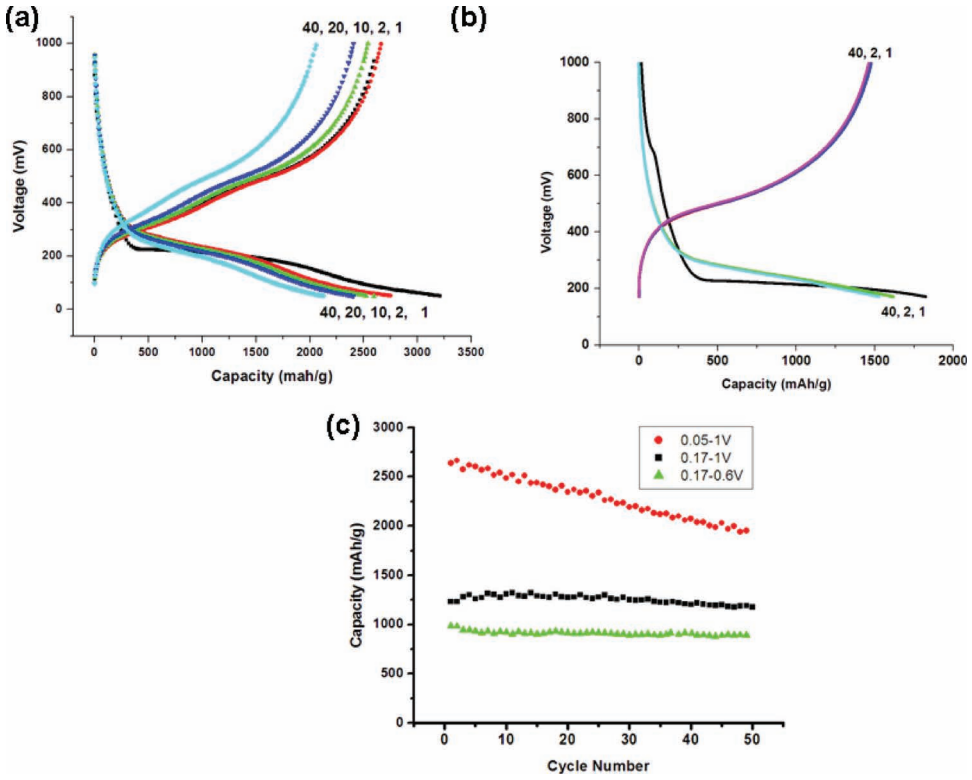

Figure 2. a) Voltage profile of a Si–CNT coaxial shell–core structure with Li metal as the counter electrode at a charge rate of *C*/5 and with an operation voltage range of 0.05–1.00 V. The numbers 1, 2, 10, 20 and 40 indicate different cycles. b) Voltage profile of a Si–CNT coaxial structure vs Li metal counter electrode at a rate of *C*/5 and an operation range of 0.17–1.0 V. c) Cycling performance of Si–CNT coaxial structures at different voltage ranges.

inelastic flow, however, does not necessarily lead to battery failure as long as good bonding is maintained between the Li/Si shell and the conductive CNT backbone. During lithiation, material in the shell is squeezed out in the radial direction via inelastic flow and the expansion of the Si shell is mostly in the radial direction (**Figure 4**a). Void formation inside the Si shell is unlikely during lithiation because the stress state is predominantly compressive. During de-lithiation, however, the axial and

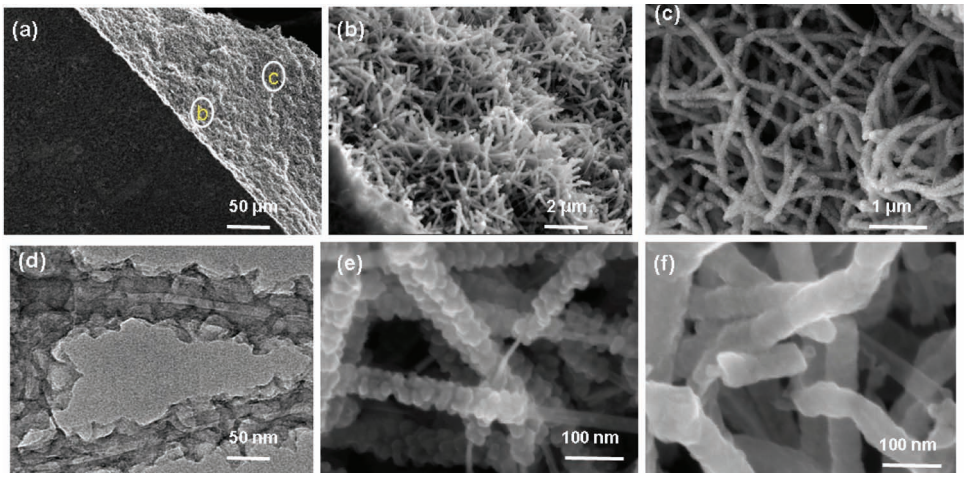

Figure 3. a) SEM image of a Si–CNT sponge film in the fully discharged state after 50 cycles. The SEI layer has been washed off with acetonitrile and 0.5 M H_2SO_4. The two circles are on the cross section of the sponge film after cutting. b) and c) show the SEM of different area as circled in (a). The cycling is uniform across the whole Si–CNT sponge film, where individual Si–CNT coaxial structure shows microporous structures with pore sizes of 10–20 nm. d) TEM of (c), where CNT cores and pores in Si are clearly seen. e) and f) show the morphologies of Si–CNT sponges after battery cycling tests with a voltage range of 0.17–1.0 and 0.17–0.6 V, respectively.

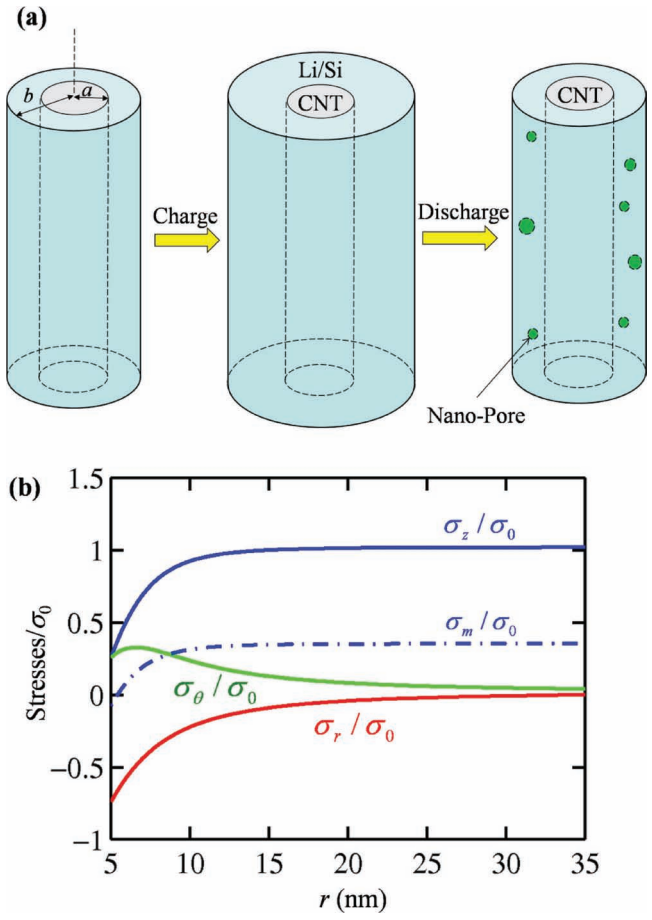

Figure 4. a) Schematic illustration of a silicon–carbon nanotube coaxial anode. During lithiation, the silicon shell expands in the radial direction through inelastic flow. During de-lithiation, nanopores form due to tensile stresses: if the radius of a nucleated pore exceeds a certain critical value, it will grow and can lead to electrode failure. b) Distribution of radial, hoop and axial stresses during de-lithation. The stresses scale with the yield strength of the material σ_0 (see the Supporting Information. The plot is generated for $a = 5$ nm, $b = 35$ nm.

hoop stresses in the NW become tensile, as shown in Figure 4b. The magnitudes of the stresses are given by:

$$\left.\begin{aligned}
\sigma_r &= -\frac{\sigma_0}{\sqrt{3}}\sinh^{-1}\left[\sqrt{3}\frac{a^2}{r^2}\right] + \frac{\sigma_0}{\sqrt{3}}\sinh^{-1}\left[\sqrt{3}\frac{a^2}{b^2}\right],\\
\sigma_\theta &= \frac{2\frac{a^2}{r^2}}{\sqrt{1+3\frac{a^4}{r^4}}}\sigma_0 - \frac{\sigma_0}{\sqrt{3}}\sinh^{-1}\left[\sqrt{3}\frac{a^2}{r^2}\right] + \frac{\sigma_0}{\sqrt{3}}\sinh^{-1}\left[\sqrt{3}\frac{a^2}{b^2}\right], \text{and}\\
\sigma_z &= \frac{1+\frac{a^2}{r^2}}{\sqrt{1+3\frac{a^4}{r^4}}}\sigma_0 - \frac{\sigma_0}{\sqrt{3}}\sinh^{-1}\left[\sqrt{3}\frac{a^2}{r^2}\right] + \frac{\sigma_0}{\sqrt{3}}\sinh^{-1}\left[\sqrt{3}\frac{a^2}{b^2}\right]
\end{aligned}\right\} \quad (1)$$

where r is the radial coordinate in a cylindrical coordinate system, a is the radius of the CNT core and b is the radius of the entire core–shell structure. σ_0 is the yielding stength of the Li/Si shell which depends on lithium concentration.[23] The tensile stress state acts as the driving force for the nucleation and growth of voids. If a nanovoid with radius ρ nucleates in the shell, competition between the driving force and the void's surface energy leads to a critical void radius ρ^*. If $\rho > \rho^*$, the void would grow into a nanopore; if $\rho < \rho^*$, the void would not grow and may heal spontaneously. Balance of stress work rate and the rate of surface energy change dictates that:

$$\rho^* = Z\frac{2\gamma}{\sigma_m} \quad (2)$$

where σ_m is the hydrostatic tensile stress, γ is the surface energy of Li/Si per unit area and Z is a dimensionless number that depends on the stress triaxiality around the void, which in turn depends on the void's location in the shell. For a void in an infinite media under pure hydrostatic loading, $Z = 1$. An accurate evaluation of Z requires numerical calculations and will be the subject of a separate paper. For simplicity, we assume Z is a constant close to unity here.

We consider two possible mechanisms that can contribute to the observed phenomenon of more voids forming when the anode is charged to 0.05 V than when charged to 0.17 V. The first mechanism is related to the concentration dependence of the surface energy γ and the yield stress σ_0 of LiSi. Although there is a lack of accurate surface energy data for Li/Si, a reasonable estimate based on Kelly's approximation suggests that $\gamma \approx Ea_0/10$, with E being the Young's modulus and a_0 being the equilibrium seperation between two neighboring atomic planes. Since the Young's modulus decreases significantly as lithium concentration c increases,[24] γ decreases with c. On the other hand, σ_m scales with the yield strength σ_0 (see Equation 1) of Li/Si, which also decreases with c.[21] If the decrease of γ is slower than the decrease of σ_m, void formation is more likely when c is dilute, and vise versa. The second mechanism leading to more voids at low c has to do with the constraining effect of SEI. In the derivation of Equation 1, traction-free boundary conditions are assumed at the outer Li/Si shell surface and surface tensions are neglected (see the Supporting Information for justification). In reality, SEI formation occurs on the LiSi surface during battery operation. Since the SEI itself does not shrink during anode delithiation, it acts as a mechanical constraint for Li/Si, adding another contribution to the tensile hydrostatic stress in Equation (1) and thereby accelerating void development. When the constraining effect of SEI adds a tensile component of σ_m^{SEI} to the total hydrostatic stress, the critical size becomes $\rho^* = 2Z\gamma/(\sigma_m + \sigma_m^{SEI})$. Both σ_m and γ decrease as lithium concentration increases, however σ_m^{SEI} does not necessarily follow the same trend. The effect of SEI, therefore, is more important when Li concentration is higher, explaining why more voids are observed in experiments when the anode is charged to 0.05 than 0.17 V. The morphological difference between Figure 3e and f, on the other hand, is more likely due to fracture of Li/Si instead of internal pore formation. For the 0.6–1 V cycling range, Li/Si is more brittle due to low Li concentrations; a senario with less effective plastic relaxation of stresses. Therefore, the deeper discharge limit (Figure 3e) of 1 V likely corresponds to a more brittle reponse of the Li/Si alloy. Since both 0.17–1.0 and 0.17–0.6 V cycling ranges demonstrate good cyclability thanks to the CNT backbone, which maintains the electrode integrity (Figure 2c), the damage at lower lithium concentrations is not analyzed here.

In summary, we have design a Si–CNT sponge structure with a large areal mass loading, 8 mg cm^{-2}. This is realized based on

the 3D porous, highly conductive CNT sponge as backbone for Si conformal deposition. The Si deposition and battery cycling were uniform over the entire CNT sponge due to the highly porous and conductive structure. When the cutoff voltage is limited from 0.05 to 0.17 V, the capacity of the electrode change from approximately 2800 to 1300 mAh g^{-1}, while the cycling retention improve dramatically. Such a capacity is still much higher than the capacity of a carbon anode. Mechanical modeling explains the cycling performance and pore formation when the cutoff voltages were set differently. When thicker CNT sponge is used, from 1 mm to 1 cm, the areal capacity could be further improved, which will be useful for MEMS power applications. With the scale up of CNT sponge fabrication and low temperature roll-to-roll Si deposition using plasma-enhanced CVD, such an Si–CNT coaxial structure with high mass loading could also be applied for next-generation energy storage for electrical vehicles.

Experimental Section

Si-CNT Sponge Synthesis: The CNT sponges were synthesized via CVD with ferrocene and 1,2-dichlorobenzene as the catalyst precursor and carbon source, and a quartz sheet as the growth substrate. A solution of ferrocene powders dissolved in dichlorobenzene (0.06 g mL^{-1}) was injected into the CVD furnace by a syringe pump at a constant feeding rate of 0.13 mL min^{-1}. The carrier gasis a mixture obtained by supplying Ar and H_2 at 2000 and 300 sccm, respectively. The reaction temperature was 860 °C and it takes 4 h for a sponge approximately 0.8 to 1 cm in thickness to reach a Si shell thickness of 30 nm around the CNT core. After deposition, the CNT sponge is peeled off the glass substrate and cut into $2 \times 2 \times 1$ mm pieces. To ensure conformal deposition of Si onto the surfaces of CNTs, the sponge was loaded into a tube furnace. The furnace was pumped to vacuum, purged with pure argon, and then heated to 490 °C. A compressed gas of 2% silane balanced in argon was flown through the furnace to produce the Si deposition onto the free-standing films of CNT sponge. Flow rates between 50 and 100 sccm were used to deliver the SiH4/Ar gas. The pressure inside the furnace was set between 40 and 100 Torr. The weight of each film was measured before and after the deposition to quantify the mass of Si which is typically around 0.5 mg. Black CNT sponges turn brown after the deposition. The Si–CNT films obtained are highly compressible, like sponges, and show excellent wetting with the electrolyte.

Li-Ion Battery Fabrication and Testing: To test the performance of the Si–CNT coaxial sponge films in batteries, coin cells were made using free-standing films as the working electrode, Celgard 2250 as the separator, and Li metal foil as the counterelectrode. The electrolyte was 1.0 M LiPF6 in 1:1 w/w ethylene carbonate/diethyl carbonate (Ferro Corporation). The cells were assembled inside an Ar-filled glovebox and sealed in aluminized polyethylene laminate bags. Galvanostatic measurements were made using a Biologic VMP3 multichannel system. The C–Si NW electrodes were cycled between 1 and 0.01 V.

Material Charaterization: Si–CNT coaxial sponge films were characterized with an FEI Sirion scanning electron microscope and a Philips CM20 transmission electron microscope. After cycling, delithiated film electrodes were taken out of the cell bags inside a glovebox, washed with acetonitrile and 0.5 M H_2SO_4 to remove the residual electrolyte and lithium salts, and dried at room temperature before subsequent SEM and TEM examinations.

Acknowledgement

L. H, H. W. and Y. G. contribute to this work equally. Y.C. acknowledges support from the King Abdullah University of Science and Technology (KAUST) Investigator Award (No. KUS-l1-001-12). Y. G. and M. Z. acknowledge support from the National Research Foundation (NRF) of Korea through World Class University (WCU) program Grant No. R31-2008-000-10083-0. A. C. acknowledges Beijing Natural Science Foundation for support (Grant 8112017: High-efficiency, recyclable nano-sponge absorption materials for water treatment).

Received: February 8, 2011
Revised: April 7, 2011

[1] R. W. Hart, H. S. White, B. Dunn, D. R. Rolison, *Electrochem. Commun.* **2003**, *5*, 120.
[2] J. W. Long, B. Dunn, D. R. Rolison, H. S. White, *Chem. Rev.* **2004**, *104*, 4463.
[3] B. A. Boukamp, G. C. Lesh, R. A. Huggins, *J. Electrochem. Soc.* **1981**, *128*, 725.
[4] D. Larcher, S. Beattie, M. Morcrette, K. Edstroem, J. C. Jumas, J. M. Tarascon, *J. Mater. Chem.* **2007**, *17*, 3759.
[5] Y. F. Gao, M. Zhou, *J. Appl. Phys.* **2011**, *109*, 014310.
[6] S. Huang, T. Zhu, *J. Power Sources* **2011**, *196*, 3664.
[7] C. K. Chan, H. L. Peng, G. Liu, K. McIlwrath, X. F. Zhang, R. A. Huggins, Y. Cui, *Nat. Nanotechnol.* **2008**, *3*, 31.
[8] M. H. Park, M. G. Kim, J. Joo, K. Kim, J. Kim, S. Ahn, Y. Cui, J. Cho, *Nano Lett.* **2009**, *9*, 3844.
[9] T. Song, J. L. Xia, J. H. Lee, D. H. Lee, M. S. Kwon, J. M. Choi, J. Wu, S. K. Doo, H. Chang, W. Il Park, D. S. Zang, H. Kim, Y. G. Huang, K. C. Hwang, J. A. Rogers, U. Paik, *Nano Lett.* **2010,** *10*, 1710.
[10] L. F. H. Cui, L. B. Cui, Yi, *ACS Nano* **2010,** *4*, 3671.
[11] J. Cho, *J. Mater. Chem.* **2010,** *20*, 4009.
[12] H. Kim, B. Han, J. Choo, J. Cho, *Angew. Chem., Int. Ed.* **2008**, *47*, 10151.
[13] J. G. Zhang, J. Liu, D. H. Wang, D. Choi, L. S. Fifield, C. M. Wang, G. Xia, Z. M. Nie, Z. G. Yang, L. R. Pederson, G. Graff, *J. Power Sources* **2010,** *195*, 1691.
[14] A. Magasinski, P. Dixon, B. Hertzberg, A. Kvit, J. Ayala, G. Yushin, *Nat. Mater.* **2010,** *9*, 353.
[15] S. Zhou, X. H. Liu, D. W. Wang, *Nano Lett.* **2010**, *10*, 860.
[16] L. F. Cui, Y. Yang, C. M. Hsu, Y. Cui, *Nano Lett.* **2009**, *9*, 3370.
[17] W. Wang, P. N. Kumta, *ACS Nano* **2010,** *4*, 2233.
[18] X. C. Gui, A. Y. Cao, J. Q. Wei, H. B. Li, Y. Jia, Z. Li, L. L. Fan, K. L. Wang, H. W. Zhu, D. H. Wu, *ACS Nano* **2010,** *4*, 2320.
[19] X. C. Gui, J. Q. Wei, K. L. Wang, A. Y. Cao, H. W. Zhu, Y. Jia, Q. K. Shu, D. H. Wu, *Adv. Mater.* **2010,** *22*, 617.
[20] J. W. Choi, J. McDonough, S. Jeong, J. S. Yoo, C. K. Chan, Y. Cui, *Nano Lett.* **2010,** *10*, 1409.
[21] V. A. Sethuraman, M. J. Chon, M. Shimshak, V. Srinivasan, P. R. Guduru, *J. Power Sources* **2010,** *195*, 5062.
[22] B. G. Demczyk, Y. M. Wang, J. Cumings, M. Hetman, W. Han, A. Zettl, R. O. Ritchie, *Mater. Sci. Eng., A* **2002**, *334*, 173.
[23] V. A. Sethuraman, M. J. Chon, M. Shimshak, V. Srinivasan, P. R. Guduru, *J. Power Sources* **2010**, *195*, 5062.
[24] V. B. Shenoy, P. Johari, Y. Qi, *J. Power Sources* **2010**, *195*, 6825.